nature physics

ARTICLES

https://doi.org/10.1038/s41567-021-01494-8

Check for updates

Cyclotron resonance overtones and near-field magnetoabsorption via terahertz Bernstein modes in graphene

D. A. Bandurin[1,6] ✉, E. Mönch[2,6], K. Kapralov[1,3], I. Y. Phinney[1], K. Lindner[2], S. Liu[4], J. H. Edgar[4], I. A. Dmitriev[2,5], P. Jarillo-Herrero[1], D. Svintsov[3] ✉ and S. D. Ganichev[2] ✉

Two-dimensional electron systems subjected to a perpendicular magnetic field absorb electromagnetic radiation via cyclotron resonance (CR). Here we report a qualitative deviation from this well-known behaviour in graphene. Our measurements of the terahertz photoresponse reveal a resonant burst at the main overtone of the CR that exceeds the signal detected at the position of the ordinary CR. The dependencies of photoresponse on the magnetic field, doping level and sample geometry suggest that the origin of this anomaly lies in the near-field magnetoabsorption facilitated by the Bernstein modes—ultraslow magnetoplasmonic excitations reshaped by non-local electron dynamics. Close to CR harmonics, these modes are characterized by a flat dispersion and diverging plasmonic density of states that amplify radiation absorption. Besides carrying fundamental interest, our results show that radiation absorption via non-local collective modes can facilitate a strong photoresponse—a behaviour potentially useful for infrared and terahertz technology.

Understanding light–matter interaction at the nanoscale is a fundamental challenge at the boundary between condensed-matter physics and nanophotonics[1]. At subwavelength scales, electromagnetic (EM) fields tend to be bound to interfaces and inhomogeneities in the material system via various collective excitations[2]. A prominent example of such excitations is plasmons, which represent coupled oscillations of charge carriers and an associated EM field. Recent years have seen a renaissance in the field of plasmonics brought on by the discovery of clean, two-dimensional electron systems (2DES)[3,4]—most prominently, graphene, with its long-lived gate-tunable plasmons[5,6]. These material platforms enable field compression by two orders of magnitude in all directions compared with free-space radiation[5], thus opening an avenue for the exploration of various quantum electrodynamic phenomena[7,8] and the development of practical infrared and terahertz (THz) devices[9,10].

The mechanisms of light–matter interaction at even smaller spatial scales (in the deep-subwavelength regime) are more intricate. They are generally governed by the non-locality of a material's current–field relation, parameterized by its non-local conductivity[11]. The non-local conductivity carries valuable information about quasiparticle dynamics[12] and interactions[13,14], inaccessible by measurements at larger spatial scales. The non-locality is also expected to smear electric fields at the smallest scales[15], thereby setting the ultimate limits to field confinement and the slowing of light in nanophotonics[16,17]. Yet, despite fundamental interest and practical importance, accessing the non-local regime of light–matter interaction has been exceedingly difficult[14,16,18,19]. This has stimulated the belief that non-local effects yield only corrections to the predictions of the local conductivity model[14,18] and therefore are routinely disregarded.

In this Article, we show that the opposite is, in fact, true and demonstrate a prominent signature of non-local light–matter interaction in a high-quality graphene device exposed to THz radiation and subjected to a classically strong magnetic field, B. The B field modifies the dispersion of two-dimensional (2D) plasmons that, at the zero wavevector q, acquires a gap (Fig. 1a) below the frequency of the electrons' cyclotron motion, ω_c (refs. [20–22]). Moreover, at large q ($\gtrsim 1/R_c$, where R_c is the cyclotron radius) and in sufficiently clean 2DES, the plasmon dispersion splits into a series of branches (Fig. 1b), an intricate behaviour that stems from the non-locality of material's conductivity, $\sigma(\mathbf{q},\omega)$ (ref. [20]). The emergent collective excitations are dubbed as Bernstein modes[23] (BMs). They were first theorized to exist in the field of plasma physics many decades ago[23,24], later explored in 2DES[20,25–28] and predicted in graphene[29]. We show that the vanishing group velocity of the BMs and large plasmonic density of states[30] facilitate strong magnetoabsorption in graphene devices in the vicinity of cyclotron resonance (CR) overtones. We detect it as a giant photoresistance peak, exceeding the signal due to the ordinary CR by a few orders of magnitude. This observation is in striking contrast with the commonly accepted scenario in which, with a few exceptions[31–33], resonant absorption at multiple CR harmonics is a weaker effect, appearing only due to non-uniform fields[34–36]. Our findings reveal the utmost importance of non-local light–matter interaction in subwavelength THz devices.

Design and characterization of the plasmonic graphene device

Our sample is a multiterminal device made of graphene encapsulated between hexagonal boron nitride (hBN) crystals that provides the best environment for high-mobility electron transport.

[1]Department of Physics, Massachusetts Institute of Technology, Cambridge, MA, USA. [2]Terahertz Center, University of Regensburg, Regensburg, Germany. [3]Center for Photonics and 2D Materials, Moscow Institute of Physics and Technology (National Research University), Dolgoprudny, Russia. [4]The Tim Taylor Department of Chemical Engineering, Kansas State University, Manhattan, KS, USA. [5]Ioffe Institute, St. Petersburg, Russia. [6]These authors contributed equally: D. A. Bandurin, E. Mönch. ✉e-mail: bandurin.d@gmail.com; svintcov.da@mipt.ru; sdg51t@gmail.com

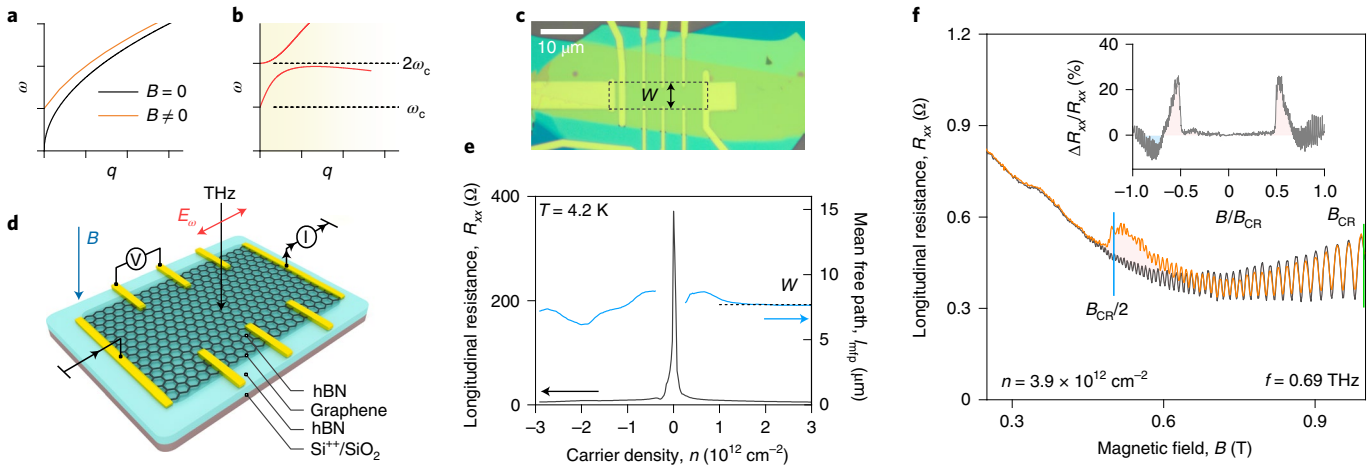

Fig. 1 | Anomalous THz photoresponse of doped graphene. a, Dispersion of plasmons in a 2DES at zero and finite B. **b**, Dispersion of BMs. At large $q \gtrsim 1/R_c$, the magnetoplasmon dispersion splits into a series of branches with anticrossing regions in the vicinity of the cyclotron frequency harmonics. **c**, Optical photograph of an encapsulated graphene device. The yellow leads are gold contacts to graphene (dashed contour) and green colour corresponds to hBN. **d**, Measurement configuration: THz radiation is incident on doped graphene subjected to a perpendicular magnetic field. The photovoltage or photoresistance is measured between different pairs of contacts. **e**, Longitudinal resistance, R_{xx}, of the device shown in **c** as a function of carrier density at 4.2 K and $B = 0$, together with the corresponding mean free path, l_{mfp}, obtained using the Drude model. **f**, Device resistance R_{xx} as a function of B measured in the dark (black curve) and in the presence of 0.69 THz radiation. The green and blue vertical lines correspond to the magnetic fields at which the CR and its second harmonics are expected at a given n. Inset, photoresistance ΔR_{xx} normalized to R_{xx} as a function of B/B_{CR} ($T = 4.2$ K).

The device was fabricated using a hot pick-up technique (Methods) and assembled on top of a Si^{++}/SiO_2 substrate that acts as a gate controlling the carrier density n (Fig. 1c). The device shape was defined by the shape of the underlying graphene flake; for this sample, the flake was about 8 μm wide and more than 30 μm long (Fig. 1c, dashed contour). To ensure the superior quality of the obtained heterostructure, we refrained from its etching into a standard Hall bar structure; instead, we left the natural graphene edge intact. The contacts were then embedded into the device channel by a combination of selective ion etching and evaporation of a thin metal layer (Methods). This configuration is particularly suitable for plasmonic experiments in which the incident radiation launches plasma waves via scattering by narrow metal contacts (~1 μm in width), thus mitigating momentum mismatch between the incident THz photons and graphene plasmons[37].

Measurements of THz magnetoabsorption in micrometre-scale systems (such as those studied in our work) cannot be performed in transmission experiments as the radiation wavelength exceeds the devices' dimensions by at least an order of magnitude. To circumvent this problem and explore radiation–matter interaction at such small scales, we employed standard methods of photoconductivity and photovoltage measurements, both performed in the Faraday configuration with the laser beam and magnetic field oriented perpendicular to the graphene plane (Fig. 1d and Methods). All our measurements were carried out in a regime far away from the quantum limit, where a large number of Landau levels are filled below the Fermi level.

Figure 1e presents the longitudinal resistance R_{xx} of our device, which reveals a standard graphene behaviour: R_{xx} peaks at the charge neutrality point (CNP) and rapidly drops on doping. Invoking the Drude model, we estimated the mean free path, l_{mfp}, of our device at $B = 0$ T (Fig. 1e, blue curve). In the high-density regime far away from the CNP, where the discussed THz-induced phenomena take place, l_{mfp} becomes close to the the device width ($W = 8$ μm), indicating micrometre-scale ballistic transport (Supplementary Section 1). At the same time, at $B \approx 0.5$ T, we observe the transition to a diffusive transport regime as follows from the observation of phonon-induced resistance oscillations as well as their complex transformation under a strong d.c. bias (Supplementary Section 1).

THz-driven magnetoresistance

Figure 1f shows the typical changes in the B dependence of longitudinal resistance R_{xx} occurring in our device in the presence of THz radiation. In the dark (black curve), the device features negative magnetoresistance for $|B| < 0.5$ T, which is followed by the Shubnikov–de Haas oscillations (SdHO) at $|B| > 0.5$ T, a standard behaviour for high-quality graphene devices (Supplementary Section 2 provides the full magnetoresistance data). When the THz radiation of frequency $f = \omega/2\pi = 0.69$ THz is turned on, the low-B behaviour of R_{xx} remains intact, whereas the SdHO amplitude gets slightly suppressed, presumably because of the radiation-induced increase in the electronic temperature to which SdHO are highly sensitive. A salient feature of the $R_{xx}(B)$ dependence measured in the presence of radiation is a pronounced resistivity spike emerging at $B \approx 0.5$ T (Supplementary Section 2 provides further examples). Figure 1f, inset, shows the difference between the orange and black curves (ΔR) that isolates this anomalous feature from the magnetoresistance background and is later referred to as the photoresistance. The strength of the effect is clearly revealed when ΔR is further normalized by R_{xx} (Fig. 1f, inset).

Strikingly, the anomalous photoresponse (Fig. 1f) peaks at magnetic field $B \simeq B_{CR}/2$ corresponding to the main CR overtone $\omega = 2\omega_c$ (Fig. 1f, blue line). At the same time, the ordinary CR at $\omega = \omega_c$ ($B \simeq B_{CR}$; Fig. 1f, green line), although allegedly being the stronger effect, was absent in the data (Fig. 1f) and only revealed itself at smaller n or higher f (Supplementary Section 3).

Characterization of photoresponse close to CR overtones

Figure 2a details our observations further by showing yet another signature of the anomalous photoresponse in the same device, but, in this case, in the photovoltage V_{ph} dependencies on B (Methods provides the measurements details). Similar to the $\Delta R(B)$ data, V_{ph} displayed very sharp and strongly asymmetric peaks and dips at $|B| \approx B_{CR}/2$ (Fig. 2a, square symbols) in a broad range of electron densities n. In Fig. 2b, we plot the experimentally determined

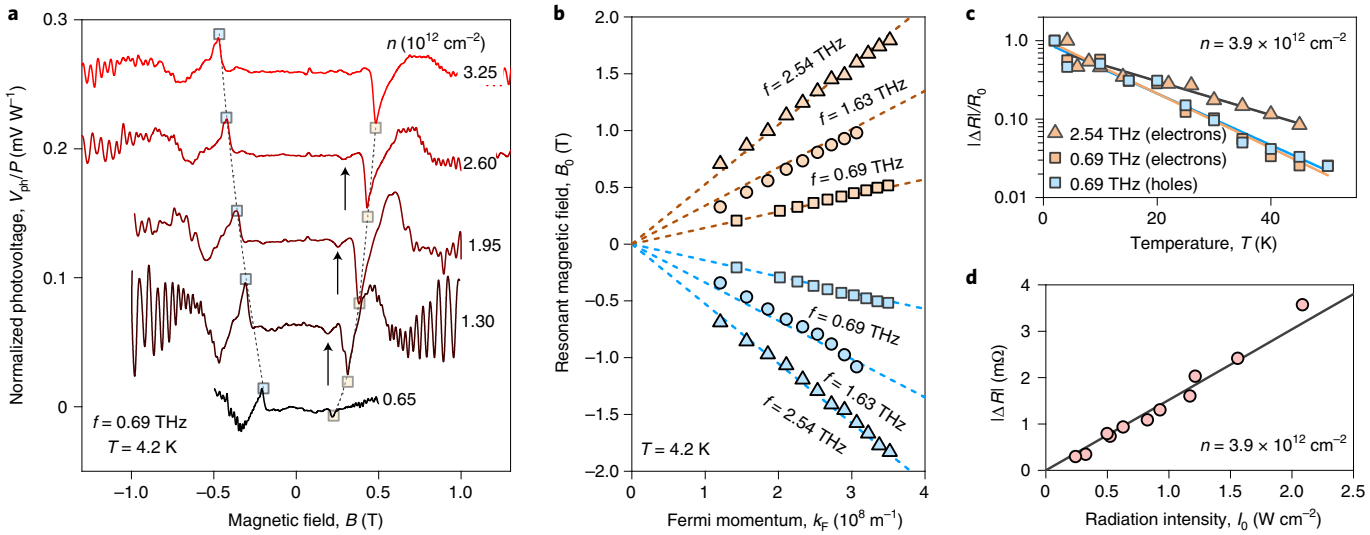

Fig. 2 | CR overtones in photovoltage and photoresistance. a, V_{ph} as a function of B for varying V_g measured in response to radiation at $f = 0.69$ THz. The square symbols (arrows) mark the features near the main (higher-order) CR overtones ($T = 4.2$ K). **b**, Resonant magnetic field B_0 of the major photovoltage (or photoresistance) peaks plotted against k_F for varying f of incoming radiation (symbols). The dashed lines denote the calculated positions of the main CR overtone ($B_{CR}/2$) as a function of k_F for a given f. The error bars stem from the uncertainty in picking the resonant magnetic field and are within the symbol size. **c**, Peak height of the resonant photoresistance (normalized to its lowest T value, R_0) as a function of T measured at $f = 0.69$ THz (squares of different colours correspond to the data taken for electrons and holes) and $f = 2.54$ THz (triangles). The solid line denotes the fits to $|\Delta R| \propto \exp(-T/T_0)$, yielding $T_0 = 12.8$ K for $f = 0.69$ THz and $T_0 = 20.1$ K for $f = 2.54$ THz. **d**, Example of the beam-intensity dependence of the resonant photoresistance recorded in response to radiation at $f = 2.54$ THz at a given n. The solid line denotes the linear fit to $|\Delta R| \propto I_0$.

positions B_0 of these sharp features versus the Fermi momentum ($k_F = \sqrt{\pi n}$), and demonstrate their linear relation. For all f, we find that positions B_0 of the anomalous features closely follow the $B_{CR}/2 = \pi f \hbar k_F / e v_F$ dependence (dashed lines), with the usual Fermi velocity of $v_F = 10^6$ m s^{-1} in high-density graphene ($\hbar$ is the Planck constant and e is the electron charge). This relation is expected from the resonant condition $\omega = 2\omega_c$, where the classical cyclotron frequency $\omega_c = eB/m$ includes the density-dependent effective cyclotron mass $m = \hbar k_F / v_F$ in graphene. This observation confirms that the photoresponse anomaly emerges close to the main CR overtone, $B_0 \approx B_{CR}/2$, for the investigated range of n and f (Supplementary Sections 2 and 3). Furthermore, similarly asymmetric yet weaker peaks in $V_{ph}(B)$ dependencies were also observed in the vicinity of the higher-order CR overtones (Fig. 2a and Supplementary Fig. 4).

With increasing temperature T, the magnitude ΔR of the resonant photoresponse at B near $B_{CR}/2$ drops (Fig. 2c). This drop follows approximately an exponential decay law ($\exp(-T/T_0)$; Fig. 2c) with the characteristic temperatures $T_0 \approx 12.8$ K for $f = 0.69$ THz and $T_0 \approx 20.1$ K for $f = 2.54$ THz. The maximum T at which the photoresistance spike was detected did not exceed 50 K. Above this temperature, the effect was fully suppressed (Supplementary Section 4 shows the detailed T dependence). Figure 2d shows the peak height $|\Delta R|$ at $B = B_0$ measured at $T = 4.2$ K as a function of laser-beam intensity I_0 and reveals their direct proportionality at low I, namely, $|\Delta R| \propto I$, with a very slight tendency to a superlinear behaviour at $I_0 > 1.5$ W cm^{-2} (Supplementary Section 6 provides the detailed I_0 dependence). This threshold-free linear behaviour excludes any instability-related mechanisms of the observed photoresponse[30] (discussed later).

We also explored the polarization dependence of the photoresponse anomalies at the CR overtones; we found that close to $B = B_{CR}/2$, the signal was neither sensitive to the polarization angle of the linearly polarized beam nor was it affected by the radiation helicity (Supplementary Section 5). This is in strong contrast to the conventional behaviour observed for ordinary CR in which the handedness of the radiation's polarization defines the magnetic-field direction at which resonant magnetoabsorption occurs.

Modelling THz magnetoabsorption

Below, we argue that the dominance of CR overtones in the THz photoresponse in our device is a signature of the magnetoabsorption assisted by the excitation of BMs in graphene. A qualitative picture of this effect is as follows. Incident EM radiation is scattered by sharp highly conductive metal contacts to the structure, producing highly non-uniform near fields with non-zero Fourier components $\mathbf{E}_{\mathbf{q}\omega}$ at large $q \approx 1/R_c$. Each spatial harmonic is screened by electrons in graphene. For harmonics close to the dispersion of magnetoplasmon modes $\mathbf{q}_{mp}(\omega)$, screening turns to anti-screening, or resonant-field enhancement. This resonant near field becomes even stronger when the group velocity of plasmons tends to zero and their density of states becomes singular. This occurs near the crossing points of the CR overtones at $\omega/\omega_c = 2, 3, \ldots$ with 'bare' plasmon dispersion $\omega_{pl}(\mathbf{q})$ obtained within the local approximation for dynamic conductivity $\sigma(q \to 0, \omega)$. Specifically, a proper account for the spatial dispersion of conductivity $\sigma(\mathbf{q}, \omega)$, which becomes relevant at $qR_c \approx 1$, leads to strong coupling and avoided crossings at the CR harmonics in the spectrum of BMs. Apart from large q, provided by the sharp contacts, BMs may only manifest themselves in a sufficiently clean system. Thus, the observed anomalies of the photoresponse attest to a superior quality of our graphene device.

The above qualitative considerations form a basis for the quantitative model of near-field absorption enhanced by graphene plasmons (Supplementary Section 6). It enables us to calculate the absorbed power P_{near} due to the scattered near fields, $\mathbf{E}_{\mathbf{q}\omega}$:

$$P_{near} = 2 \int \frac{d\mathbf{q}}{(2\pi)^2} \frac{\omega}{2\pi q} |\mathbf{E}_{\mathbf{q}\omega}|^2 \, \mathrm{Im} \, \frac{1}{\varepsilon(\mathbf{q}, \omega)}. \quad (1)$$

In the above expression, $\mathbf{E}_{\mathbf{q}\omega} = F_{\mathbf{q}\omega} \mathbf{E}_0$ is the amplitude of the $\mathbf{q}$th spatial harmonic of the electric near field, which is related to the

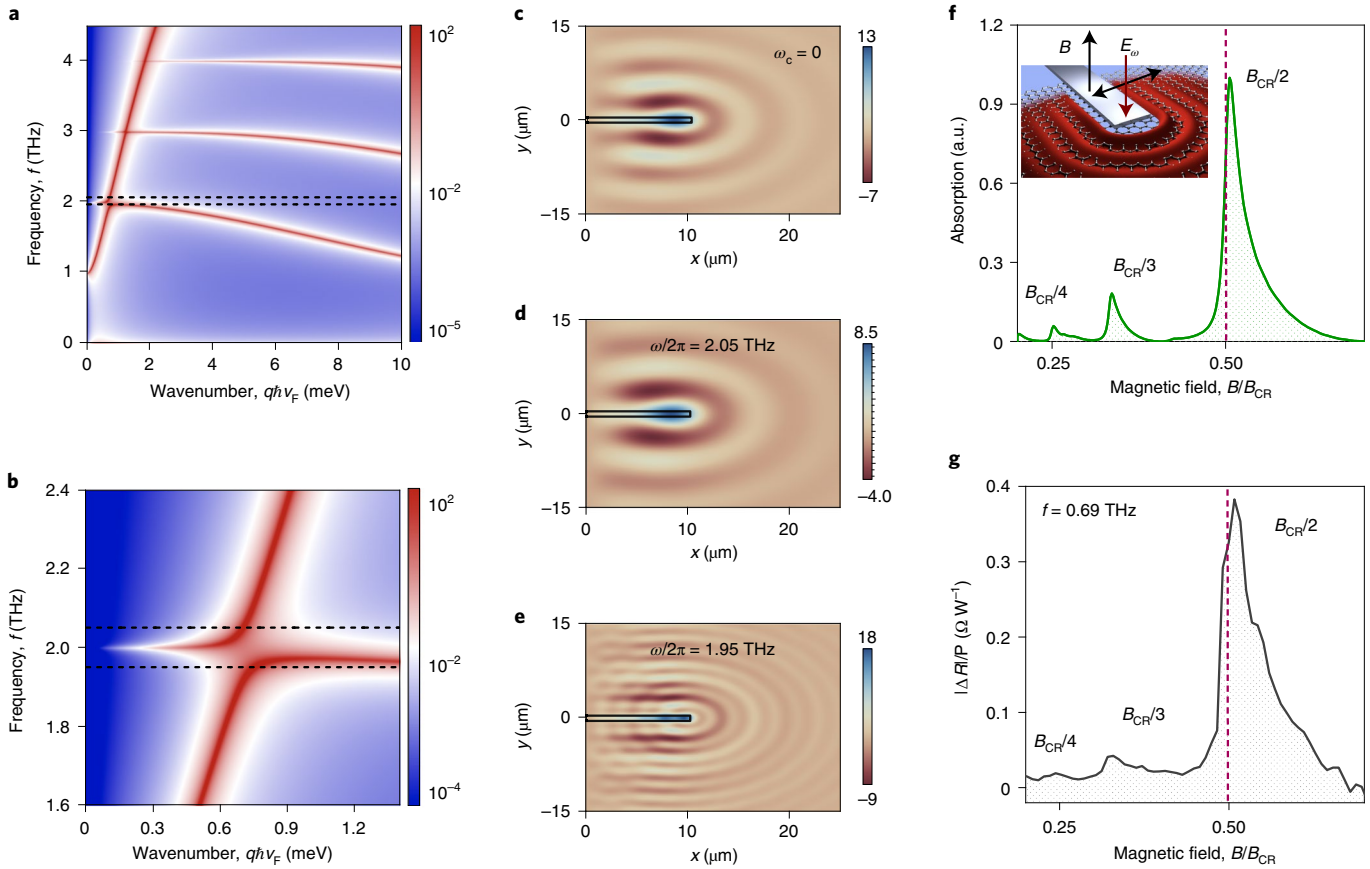

Fig. 3 | Non-local THz magnetoabsorption in graphene. a, Loss function $\mathrm{Im}\,\varepsilon^{-1}(\mathbf{q},\omega)$ in the presence of a magnetic field calculated for $\omega_c/2\pi = 1$ THz with a perfectly conducting metal gate. The dashed horizontal lines correspond to the frequencies $\omega/2\pi$ from the simulations (**d** and **e**). **b**, Zoomed-in region of **a** in the vicinity of the main CR overtone. **c**–**e**, Numerical simulations of the near-field distribution of THz graphene plasmons (**c**) and BMs above (**d**) and below (**e**) the cyclotron gap excited by a metal lead located in contact with the graphene sheet placed above the silicon gate at $\omega_c/2\pi = 1$ THz for $n = 0.6\times10^{12}$ cm^{-2}. The colour scales visualize the real part of the vertical field component, namely, $\mathrm{Re}\,E_z(x, y)$. **f**, Calculated BM-assisted absorption of THz radiation as a function of B normalized to B_{CR}. Inset, model structure of the graphene–metal interface that was used for the calculations (Supplementary Section 6). **g**, Photoresistance in the vicinity of the CR overtones measured at $f = 0.69$ THz.

incident field $\mathbf{E}_0$ via the diffraction amplitude $F_{\mathbf{q}\omega}$, and $\varepsilon(\mathbf{q},\omega)$ is the momentum- and frequency-dependent dielectric function of graphene (Supplementary Section 7). The so-called 'loss function', namely, $\mathrm{Im}\,\varepsilon^{-1}(\mathbf{q},\omega)$, is responsible for magnetoplasmon-assisted absorption. It peaks at the collective mode dispersion (Fig. 3a,b). The analysis of the collective mode contribution to the net power (equation (1)) shows that it is inversely proportional to the magnetoplasmon group velocity at that frequency, that is, $v_{gr}(\omega)$. In the immediate vicinity of the anti-crossings, the group velocity approaches zero (Fig. 3a,b and Supplementary Section 8). Here the absorption is limited by the plasmon losses and the associated electron momentum relaxation time, τ_p, as $P_{near} \propto \tau_p^{1/2}$ (Supplementary Section 8).

The evaluation of the absorbed power for specific structure parameters requires the knowledge of two building blocks: diffraction amplitude $F_{\mathbf{q}\omega}$ and dielectric function $\varepsilon(\mathbf{q},\omega)$. The former is evaluated by considering plane-wave scattering by a perfectly conducting rod that mimics a sharp contact (Supplementary Section 6). The respective diffraction amplitude tends to zero at small q due to gate screening, reaches a maximum and tends to zero at large q due to the finite length and width of the contact. The dielectric function $\varepsilon(\mathbf{q},\omega)$ is directly linked to $\sigma(\mathbf{q},\omega)$ that was evaluated using a classical kinetic equation with weak particle-conserving collisions (Supplementary Section 7). The calculated loss function demonstrates well-defined BMs (Fig. 3a,b).

To provide a more detailed picture of the BM resonance, we further show the real-space distributions of the scattered electric field in different regimes (Fig. 3c–e). At zero magnetic field (Fig. 3c) and away from the BM plateau at $\omega \approx 2\omega_c$ (Fig. 3d), contacts launch (magneto)plasmons with a well-defined real-space period of the electric field corresponding to wavevector $q_{mp}(\omega)$ (ref. [37]). In contrast, just below the maximum of the BM dispersion, there exist two magnetoplasmon modes with different q values at a given radiation frequency (Fig. 3a,b). This results in the short-period fringing of the electric field threaded on the long-period pattern (Fig. 3e). Exactly at the BM plateau, the two periods coalesce, leading to resonance enhancement of the net absorbance (Supplementary Video 1).

Discussion

In Fig. 3f,g, we compare the experimentally measured photoresistance and calculated magnetoabsorption (Supplementary Section 8) in the vicinity of the main CR overtones and find a good qualitative agreement. In particular, both dependencies feature strong asymmetry of resonant peaks characterized by a rapid growth on the low-B sides of the CR overtones (similar to Figs. 1d and 2a). The reason for this asymmetry becomes clear when one realizes that the steep rise (at a shorter scale related to scattering losses) corresponds to external frequency ω approaching the maximum of BM dispersion from the gap side. The smooth drop at $B > B_{CR}/2$ reflects the

gradual increase in the group velocity of the participating BMs for ω below the maximum (Fig. 3e). At that side, one returns to the conventional magnetoplasmon excitation regime (Fig. 3d) where the non-locality, although present, does not play any essential role.

Importantly, the asymmetry in the magnetoabsorption curves retains for the third and fourth harmonics of the CR in both experimental and theoretical curves (Fig. 3f,g). This behaviour clearly distinguishes the BM resonances from THz-induced magneto-oscillations recently found in high-quality graphene—these oscillations are readily described by a damped sinusoidal function in the limit of the B range applied in this work[38]. In this device, signatures of such sinusoidal magneto-oscillations appear only at higher f (Supplementary Section 3).

The key role in the excitation of BMs, similar to the other collective modes in two dimensions, should be played by the inhomogeneity of electric fields due to the presence of sharp contacts. To verify the idea, we have fabricated an additional device of comparable quality but contacted by metal leads outside the main channel (Supplementary Section 10). We found strong photoresponse in the vicinity of the CR harmonics only for the invasive case, whereas for distant leads, the photoresponse was dominated by THz-induced magneto-oscillations[38].

It is remarkable that the photovoltage and photoresistance at the main CR overtone can markedly exceed that at the CR itself. Moreover, the fundamental resonance is observed only at low carrier densities or high f (Supplementary Sections 3 and 9). The softening of the fundamental CR at large n can be understood by taking into account the screening of incoming radiation by electrons in graphene, a dissipationless effect also referred to as radiative damping[39–42]. Calculations of the fundamental CR absorption based on the transfer-matrix technique are shown in Supplementary Fig. 18 and this effect is well captured. Absorption at CR overtones is not prone to screening; instead, it is enhanced by the near-field excitation of BMs. The observed decay of the second CR with an increasing gate voltage is relatively weak. This can be attributed to the reduced characteristic values of magnetoplasmon wavevector $q^{\star}$ and the respective decrease in diffraction amplitude $F_{\mathbf{q}\omega}$.

It is instructive now to briefly mention the possible mechanisms responsible for the conversion of absorbed radiation into electrical signals. We attribute the positive photoresistance to strong radiation-induced heating and thus enhanced electron scattering. Indeed, in the presence of THz radiation, the amplitude of SdHO gets suppressed, which is a clear signature of the increased electronic temperature (Fig. 1f). The results obtained in the photovoltage configuration are more intricate as $V_{\mathrm{ph}}(B)$ dependencies were found odd in B for $f=0.69$ THz and thus can signal the THz-induced Nernst effect. Last, the observed exponential damping of the measured photoresponse with T (Fig. 2c) eludes interpretation within the adopted quasiclassical model presented in the Supplementary Information and requires detailed knowledge on the mechanisms of THz downconversion into d.c. signals.

Finally, below, we discuss the other possible scenarios of the resonant photoresponse at CR overtones. In particular, similar resonances were predicted to emerge in the regime of viscous electron transport[43]. The aforementioned photoresponse asymmetry in our theory and experiments is, however, opposite to that obtained elsewhere[43], which predicts a smooth low-B tail and sharp high-B tail of the magnetoabsorption peak at around $B=B_{\mathrm{CR}}/2$. Moreover, the hydrodynamic regime of electron transport in high-density graphene sets in at $T>100$ K (ref. [44]), whereas the CR harmonics observed in this work disappear at $T\approx 50$ K (Fig. 2c and Supplementary Section 4). We have also addressed the effect of electron–electron (e–e) collisions on the BM-assisted magnetoabsorption and found that a fast collision rate causes a reduction in the amplitudes of CR harmonics (Supplementary Section 6). Next, we note that although BMs were discussed in relation to the resonant photoresistance close to the second CR harmonics observed in GaAs-based heterostructures[31], the described scenario relied on the emergence of electron plasma instability[30]. The effect described here is linear in P, which excludes any instability-related mechanisms. The same observation also excludes multiphoton mechanisms that would inevitably lead to nonlinear scaling with P (ref. [45]). Last, since our experiments were performed at relatively large n and small f, the observed anomalies cannot be possibly related to interband radiation absorption that is routinely observed in graphene close to the CNP[46] (Supplementary Section 2).

Outlook

The observed resonant THz absorption has several profound consequences for further research on light–matter interaction at the nanoscale. First, the interaction between graphene plasmons and electron cyclotron motion via the formation of BMs and mediated by non-locality effects can easily reach the strong-coupling regime[47,48]. Indeed, the BM gap due to resonant anticrossing can be estimated as $\Delta\approx 10(a_{\mathrm{B}}/R_{\mathrm{c}})^2\omega_{\mathrm{c}}$, where a_{B} is the effective Bohr radius[30]. Taking $f=1.63$ THz, we find that $\Delta/\omega_{\mathrm{c}}\approx 0.17$, which is well beyond the collision-induced broadening of resonance. In this regime, electron relaxation from higher Landau levels may demonstrate coherent quantum Rabi oscillations that can be potentially detected in time-resolved measurements[49]. Second, ultraslow collective excitations associated with BMs close to the CR harmonics can be sensitive to many-body effects[50]. Our approach, thus, paves the way to access these effects in photoresponse experiments. Third, our non-local measurement scheme can be envisioned as a potential tool to probe electron Hall viscosity, an important transport coefficient that until recently was disregarded in low-dimensional systems[44,51]. Last, our observations revisit the role of non-local conductivity in light–matter interaction, which was previously believed to hamper field compression and slowing of light[11]. Our study refutes this perspective by revealing highly confined ultraslow plasmon modes enabled by non-locality.

Online content

Any methods, additional references, Nature Research reporting summaries, source data, extended data, supplementary information, acknowledgements, peer review information; details of author contributions and competing interests; and statements of data and code availability are available at https://doi.org/10.1038/s41567-021-01494-8.

Received: 31 May 2021; Accepted: 14 December 2021;
Published online: 07 February 2022

References

1. Novotny, L. & Hecht, B. *Principles of Nano-optics* (Cambridge Univ. Press, 2012).
2. Basov, D. N., Fogler, M. M. & García de Abajo, F. J. Polaritons in van der Waals materials. *Science* **354**, aag1992 (2016).
3. Gusikhin, P. A., Muravev, V. M., Zagitova, A. A. & Kukushkin, I. V. Drastic reduction of plasmon damping in two-dimensional electron disks. *Phys. Rev. Lett.* **121**, 176804 (2018).
4. Geiser, M. et al. Ultrastrong coupling regime and plasmon polaritons in parabolic semiconductor quantum wells. *Phys. Rev. Lett.* **108**, 106402 (2012).
5. Ni, G. et al. Fundamental limits to graphene plasmonics. *Nature* **557**, 530–533 (2018).
6. Woessner, A. et al. Highly confined low-loss plasmons in graphene–boron nitride heterostructures. *Nat. Mater.* **14**, 421–425 (2015).
7. Reserbat-Plantey, A. et al. Quantum nanophotonics in two-dimensional materials. *ACS Photonics* **8**, 85–101 (2021).
8. Silveiro, I., Ortega, J. M. P. & de Abajo, F. J. G. Quantum nonlocal effects in individual and interacting graphene nanoribbons. *Light Sci. Appl.* **4**, e241 (2015).
9. Muravev, V. M. & Kukushkin, I. V. Plasmonic detector/spectrometer of subterahertz radiation based on two-dimensional electron system with embedded defect. *App. Phys. Lett.* **100**, 082102 (2012).

10. Bandurin, D. A. et al. Resonant terahertz detection using graphene plasmons. *Nat. Commun.* **9**, 5392 (2018).
11. Ciracì, C. et al. Probing the ultimate limits of plasmonic enhancement. *Science* **337**, 1072–1074 (2012).
12. Gonçalves, P. A. D. et al. Quantum surface-response of metals revealed by acoustic graphene plasmons. *Nat. Commun.* **12**, 3271 (2021).
13. Rostami, H., Katsnelson, M. I. & Polini, M. Theory of plasmonic effects in nonlinear optics: the case of graphene. *Phys. Rev. B* **95**, 035416 (2017).
14. Lundeberg, M. B. et al. Tuning quantum nonlocal effects in graphene plasmonics. *Science* **357**, 187–191 (2017).
15. Pendry, J. B., Huidobro, P. A., Luo, Y. & Galiffi, E. Compacted dimensions and singular plasmonic surfaces. *Science* **358**, 915–917 (2017).
16. Alcaraz Iranzo, D. et al. Probing the ultimate plasmon confinement limits with a van der Waals heterostructure. *Science* **360**, 291–295 (2018).
17. Koshelev, K. L. & Bogdanov, A. A. Interplay between anisotropy and spatial dispersion in metamaterial waveguides. *Phys. Rev. B* **94**, 115439 (2016).
18. Nehls, J. et al. Direct manifestation of the Fermi pressure in a two-dimensional electron system. *Phys. Rev. B* **54**, 7651–7653 (1996).
19. Koitzsch, A. et al. Nonlocal dielectric function and nested dark excitons in MoS_2. *npj 2D Mater. Appl.* **3**, 41 (2019).
20. Chiu, K. W. & Quinn, J. J. Plasma oscillations of a two-dimensional electron gas in a strong magnetic field. *Phys. Rev. B* **9**, 4724–4732 (1974).
21. Yan, H. et al. Infrared spectroscopy of tunable Dirac terahertz magneto-plasmons in graphene. *Nano Lett.* **12**, 3766–3771 (2012).
22. Crassee, I. et al. Intrinsic terahertz plasmons and magnetoplasmons in large scale monolayer graphene. *Nano Lett.* **12**, 2470–2474 (2012).
23. Bernstein, I. B. Waves in a plasma in a magnetic field. *Phys. Rev.* **109**, 10–21 (1958).
24. Sitenko, A. & Stepanov, K. On the oscillations of an electron plasma in a magnetic field. *Soviet Phys. JETP* **4**, 512 (1957).
25. Batke, E., Heitmann, D., Kotthaus, J. P. & Ploog, K. Nonlocality in the two-dimensional plasmon dispersion. *Phys. Rev. Lett.* **54**, 2367–2370 (1985).
26. Gudmundsson, V. et al. Bernstein modes in quantum wires and dots. *Phys. Rev. B* **51**, 17744–17754 (1995).
27. Batke, E., Heitmann, D. & Tu, C. W. Plasmon and magnetoplasmon excitation in two-dimensional electron space-charge layers on GaAs. *Phys. Rev. B* **34**, 6951–6960 (1986).
28. Holland, S. et al. Quantized dispersion of two-dimensional magnetoplasmons detected by photoconductivity spectroscopy. *Phys. Rev. Lett.* **93**, 186804 (2004).
29. Roldán, R., Goerbig, M. O. & Fuchs, J.-N. Theory of Bernstein modes in graphene. *Phys. Rev. B* **83**, 205406 (2011).
30. Volkov, V. A. & Zabolotnykh, A. A. Bernstein modes and giant microwave response of a two-dimensional electron system. *Phys. Rev. B* **89**, 121410 (2014).
31. Dai, Y., Du, R. R., Pfeiffer, L. N. & West, K. W. Observation of a cyclotron harmonic spike in microwave-induced resistances in ultraclean GaAs/AlGaAs quantum wells. *Phys. Rev. Lett.* **105**, 246802 (2010).
32. Hatke, A. T., Zudov, M. A., Pfeiffer, L. N. & West, K. W. Giant microwave photoresistivity in high-mobility quantum Hall systems. *Phys. Rev. B* **83**, 121301 (2011).
33. Dorozhkin, S. I., Kapustin, A. A., Umansky, V. & Smet, J. H. Absorption of microwave radiation by two-dimensional electron systems associated with the excitation of dimensional Bernstein mode resonances. *JETP Lett.* **113**, 670–675 (2021).
34. Chaplik, A. V. & Heitmann, D. Geometric resonances of two-dimensional magnetoplasmons. *J. Phys. C: Solid State Phys.* **18**, 3357–3363 (1985).
35. Bangert, D. E., Stuart, R. J., Hughes, H. P., Ritchie, D. A. & Frost, J. E. F. Bernstein modes in grating-coupled 2DEGs. *Semicond. Sci. Technol.* **11**, 352–359 (1996).
36. Białek, M., Łusakowski, J., Czapkiewicz, M., Wróbel, J. & Umansky, V. Photoresponse of a two-dimensional electron gas at the second harmonic of the cyclotron resonance. *Phys. Rev. B* **91**, 045437 (2015).
37. Alonso-González, P. et al. Controlling graphene plasmons with resonant metal antennas and spatial conductivity patterns. *Science* **344**, 1369–1373 (2014).
38. Mönch, E. et al. Observation of terahertz-induced magnetooscillations in graphene. *Nano Lett.* **20**, 5943–5950 (2020).
39. Fal'ko, V. I. & Khmel'nitskii, D. E. What if a film conductivity exceeds the speed of light? *Soviet Phys. JETP* **68**, 1150–1152 (1989).
40. Mikhailov, S. A. Microwave-induced magnetotransport phenomena in two-dimensional electron systems: importance of electrodynamic effects. *Phys. Rev. B* **70**, 165311 (2004).
41. Andreev, I. V., Muravev, V. M., Belyanin, V. N. & Kukushkin, I. V. Measurement of cyclotron resonance relaxation time in the two-dimensional electron system. *Appl. Phys. Lett.* **105**, 202106 (2014).
42. Zhang, Q. et al. Superradiant decay of cyclotron resonance of two-dimensional electron gases. *Phys. Rev. Lett.* **113**, 047601 (2014).
43. Alekseev, P. S. & Alekseeva, A. P. Transverse magnetosonic waves and viscoelastic resonance in a two-dimensional highly viscous electron fluid. *Phys. Rev. Lett.* **123**, 236801 (2019).
44. Berdyugin, A. I. et al. Measuring Hall viscosity of graphene's electron fluid. *Science* **364**, 162–165 (2019).
45. Dmitriev, I. A., Mirlin, A. D., Polyakov, D. G. & Zudov, M. A. Nonequilibrium phenomena in high Landau levels. *Rev. Mod. Phys.* **84**, 1709–1763 (2012).
46. Orlita, M. et al. Carrier scattering from dynamical magnetoconductivity in quasineutral epitaxial graphene. *Phys. Rev. Lett.* **107**, 216603 (2011).
47. Scalari, G. et al. Ultrastrong coupling of the cyclotron transition of a 2D electron gas to a THz metamaterial. *Science* **335**, 1323–1326 (2012).
48. Muravev, V. M., Gusikhin, P. A., Andreev, I. V. & Kukushkin, I. V. Ultrastrong coupling of high-frequency two-dimensional cyclotron plasma mode with a cavity photon. *Phys. Rev. B* **87**, 045307 (2013).
49. Zhang, Q. et al. Superradiant decay of cyclotron resonance of two-dimensional electron gases. *Phys. Rev. Lett.* **113**, 047601 (2014).
50. Levitov, L. S., Shtyk, A. V. & Feigelman, M. V. Electron-electron interactions and plasmon dispersion in graphene. *Phys. Rev. B* **88**, 235403 (2013).
51. Sherafati, M., Principi, A. & Vignale, G. Hall viscosity and electromagnetic response of electrons in graphene. *Phys. Rev. B* **94**, 125427 (2016).

Publisher's note Springer Nature remains neutral with regard to jurisdictional claims in published maps and institutional affiliations.

© The Author(s), under exclusive licence to Springer Nature Limited 2022

Methods

Device fabrication. To fabricate our devices, we first encapsulated graphene between relatively thick hBN crystals using a hot-release technique[52]. The stack was transferred either on top of a predefined back-gate electrode made of graphite or onto a Si^{++}/SiO_2 wafer. The resulting van der Waals heterostructure was patterned using electron-beam lithography to define the contact regions, which was followed by reactive ion etching to selectively remove the areas unprotected by a lithographic mask, resulting in trenches for depositing electrical leads (gold/chromium, 70/3 nm). For one of our devices, we used rectangular-shaped graphene flakes forming the device channel, whereas for another device, the graphene channel was defined by a third round of electron-beam lithography, followed by reactive ion etching using poly(methyl methacrylate) and a gold top gate as the etching mask.

Measurement technique. The sample was mounted within a variable-temperature inset of an optical cryostat equipped with *z*-cut crystal quartz windows, which were covered by a black polyethylene film. Although the latter is transparent for THz radiation, the polyethylene film functions as a filter in both visible and infrared ranges, preventing uncontrollable excitation of graphene by room light. The homogeneous magnetic field (B) was generated by superconductive coils in the range of ± 7 T. Standard four-terminal magnetotransport measurements were performed using a.c. currents between 1 and 5 μA, providing information about the sample's transport characteristics and quality.

Our high-quality graphene devices were investigated under several frequencies, namely, $f = 0.69$, 1.63 and 2.54 THz, with the corresponding photon energies ($\hbar\omega$) of 2.9, 6.7 and 10.5 meV, generated by a continuous-wave optically pumped molecular laser using CH_2O_2, CH_2F_2 and CH_3OH, respectively, as the active media. The laser beam was recorded by a pyroelectric camera[53], which showed a nearly Gaussian profile with full-width-at-half-maximum spot diameters (d_s) of 2.58, 1.75 and 1.56 mm at the sample's position. The incident average powers (P) were in the range from 15 to 80 mW, providing intensities ($I_0 = P/A_s$) of up to 3.32 W cm^{-2} (refs. [54,55]). The state of the initially linearly polarized radiation was controlled in angle and ellipticity by the rotation of the waveplates made of *x*-cut crystal quartz. All the measurements were performed in Faraday geometry, where both magnetic field and incoming THz radiation were perpendicular to the graphene plane.

Measurements of THz magnetoabsorption in the deep-subwavelength regime cannot be performed in transmission experiments. To explore radiation–matter interaction at such small spatial scales, we used standard methods of photoconductivity and photovoltage measurements. Since photoconductivity bursts and photovoltage generation appear due to THz absorption, both types of measurement enabled us to reveal all the characteristic features of the absorption processes. Indeed, photoconductivity and photovoltage are proportional to the absorbed EM power multiplied by some 'sensitivity function', which encodes microscopic mechanisms of power-to-electrical-signal conversion. This function usually does not distort the sharp and narrow absorption peaks in plasmonic experiments[10,14].

In the photovoltage regime, the induced signal was measured as a voltage drop V_{ph} between a pair of contacts without applying an external bias to the device. The incident radiation was modulated by an optical chopper to provide phase-sensitive detection with a standard lock-in technique. To obtain a photoresistance signal, that is, a change in d.c. conductivity induced by THz radiation, an a.c. current ($I_{a.c.}$) between 5 and 50 μA was applied to the device with a modulation frequency lying within the range of $f_{a.c.} = 5$–12 Hz, whereas the sample was exposed to laser radiation simultaneously modulated at a significantly larger frequency of $f_{chop} = 140$ Hz (ref. [56]). Such a double-modulation measurement technique is realized via two lock-in amplifiers connected in series. Here the first lock-in amplifier is phase locked to f_{chop}, extracting the total signal induced by THz radiation. The amplitude of the total photosignal, oscillating at f_{chop}, includes a constant component proportional to the photovoltage and an alternating part modulated with $f_{a.c.}$. This total signal feeds the second amplifier that is locked to $f_{a.c.}$, thus generating a voltage proportional to the photoresistance. We also note that in contrast to photoresistance, the photovoltage may change its sign on reversing the direction of B. Indeed, the magnetic field can determine a preferential direction for V_{ph} generation in the structure, for instance, the case of THz-induced Nernst effect.

THz absorption modelling. The absorption cross section was evaluated using Joule's law relating the absorbed power, real part of dynamic 2D conductivity and local electric field. The wavevector-dependent dynamic conductivity was obtained by solving the classical kinetic equation for a 2D electron gas in a magnetic field in the presence of weak disorder[34]. The resulting expression for $\sigma(\mathbf{q}, \omega)$ is a sum of terms resonant at various CR overtones, with q-dependent amplitudes. Electron–impurity collisions were included in a particle-conserving way; for e–e collisions, we used a model particle- and momentum-conserving collision integral[57]. The electric field acting on the electrons in graphene is a sum of an incident plane wave and evanescent wave scattered by the keen contact. The amplitude and shape of the evanescent wave were found by solving the scattering problem for a conducting rod[58]. Both plane- and evanescent-wave amplitudes are modified due to screening by electrons in graphene. As a result, each $\mathbf{q}$th spatial harmonic of the field is divided by a 2D dielectric function $\varepsilon(\mathbf{q}, \omega) = 1 + 2\pi i\sigma(\mathbf{q}, \omega)\sqrt{q^2 - k_0^2}/\omega$, where $k_0 = \omega/c$ is the wavenumber of the incident wave. The effective dielectric function modified by the presence of the encapsulating dielectric and gate is given in Supplementary Section 6.

Data availability

The data reported in Figs. 1–3 can be found on Zenodo (https://doi.org/10.5281/zenodo.5758483). The other data that support the findings of this study are available from the corresponding authors upon reasonable request.

References

52. Purdie, D. G. et al. Cleaning interfaces in layered materials heterostructures. *Nat. Commun.* **9**, 5387 (2018).
53. Ziemann, E., Ganichev, S. D., Prettl, W., Yassievich, I. N. & Perel, V. I. Characterization of deep impurities in semiconductors by terahertz tunneling ionization. *J. Appl. Phys.* **87**, 3843–3849 (2000).
54. Olbrich, P. et al. Terahertz ratchet effects in graphene with a lateral superlattice. *Phys. Rev. B* **93**, 075422 (2016).
55. Dantscher, K.-M. et al. Photogalvanic probing of helical edge channels in two-dimensional HgTe topological insulators. *Phys. Rev. B* **95**, 201103 (2017).
56. Kozlov, D. A., Kvon, Z. D., Mikhailov, N. N., Dvoretskii, S. A. & Portal, J. C. Cyclotron resonance in a two-dimensional semimetal based on a HgTe quantum well. *JETP Lett.* **93**, 170–173 (2011).
57. Svintsov, D. Hydrodynamic-to-ballistic crossover in Dirac materials. *Phys. Rev. B* **97**, 121405 (2018).
58. Hallén, E. Properties of a long antenna. *J. Appl. Phys.* **19**, 1140–1147 (1948).

Acknowledgements

E.M., K.L., I.A.D. and S.D.G. acknowledge the support of the Deutsche Forschungsgemeinschaft (DFG, German Research Foundation) under Project ID 314695032 and SFB 1277 (Subproject A04). I.A.D. acknowledges DFG support via grant DM 1/5-1. Work at MIT was partly supported through AFOSR grant FA9550-21-1-0319, NSF QII-TAQS program (grant 1936263) and Gordon and Betty Moore Foundation EPiQS Initiative through grant GBMF9643 to P.J.-H. D.A.B. acknowledges support from the MIT Pappalardo Fellowship. I.Y.P. acknowledges support from the MIT undergraduate research opportunities program and the Johnson & Johnson research scholars program. Support from the Materials Engineering and Processing program of the National Science Foundation under award no. CMMI 1538127 for hBN crystal growth is also greatly appreciated. The work of D.S. was supported by the Foundation for Advancement of Theoretical Physics 'Basis' under grant no. 20-1-3-43-1. K.K. and D.S. acknowledge financial support from the Ministry of Science and Higher Education of the Russian Federation (agreement no. 075-15-2021-606). We thank L. Levitov, C. Collignon, A. Berdyugin, A. Principi, A. Bogdanov and A. A. Zibrov for valuable discussions.

Author contributions

D.A.B., D.S. and S.D.G conceived and designed the project. E.M., D.A.B. and K.L. performed the transport and photoresponse measurements at the University of Regensburg. D.A.B. and I.Y.P. fabricated the devices. D.A.B., E.M., I.A.D. and D.S. analysed the experimental data with help from P.J.-H. and S.D.G. K.K. and D.S. developed the theoretical model and performed the magnetoabsorption calculations. S.L. and J.H.E. provided the high-quality hBN crystals. D.A.B., I.A.D., E.M. and D.S. wrote the manuscript, with input from all the co-authors. P.J.-H. and S.D.G. supervised the project. All the authors contributed to discussions.

Competing interests

The authors declare no competing interests.

Additional information

Supplementary information The online version contains supplementary material available at https://doi.org/10.1038/s41567-021-01494-8.

Correspondence and requests for materials should be addressed to D. A. Bandurin, D. Svintsov or S. D. Ganichev.

Peer review information *Nature Physics* thanks the anonymous reviewers for their contribution to the peer review of this work.

Reprints and permissions information is available at www.nature.com/reprints.